RESEARCH ARTICLE

A continuous net-like eutectic structure enhances the corrosion resistance of Mg alloys

Cijun Shuai[1,2,3], Wenjing Yang[1,2], Youwen Yang[2], Chengde Gao[1], Chongxian He[2]*, Hao Pan[4]*

[1]State Key Laboratory of High Performance Complex Manufacturing, College of Mechanical and Electrical Engineering, Central South University, Changsha 410083, People's Republic of China
[2]Jiangxi University of Science and Technology, Ganzhou 341000, People's Republic of China
[3]Shenzhen Institute of Information Technology, Shenzhen 518172, People's Republic of China
[4]Department of Periodontics and Oral Mucosal Section, Xiangya Stomatological Hospital, Central South University, Changsha 410078, People's Republic of China

Abstract: Mg alloys degrade rather rapidly in a physiological environment, although they have good biocompatibility and favorable mechanical properties. In this study, Ti was introduced into AZ61 alloy fabricated by selective laser melting, aiming to improve the corrosion resistance. Results indicated that Ti promoted the formation of Al-enriched eutectic α phase and reduced the formation of β-$Mg_{17}Al_{12}$ phase. With Ti content reaching to 0.5 wt.%, the Al-enriched eutectic α phase constructed a continuous net-like structure along the grain boundaries, which could act as a barrier to prevent the Mg matrix from corrosion progression. On the other hand, the Al-enriched eutectic α phase was less cathodic than β-$Mg_{17}Al_{12}$ phase in AZ61, thus alleviating the corrosion progress due to the decreased potential difference. As a consequence, the degradation rate dramatically decreased from 0.74 to 0.24 $mg \cdot cm^{-2} \cdot d^{-1}$. Meanwhile, the compressive strength and microhardness were increased by 59.4% and 15.6%, respectively. Moreover, the Ti-contained AZ61 alloy exhibited improved cytocompatibility. It was suggested that Ti-contained AZ61 alloy was a promising material for bone implants application.

Keywords: eutectic α phase; net-like structure; selective laser melting; mg alloys; corrosion resistance

*Correspondence to: Dr. Chongxian He, Jiangxi University of Science and Technology, Ganzhou 341000, People's Republic of China; Tel: +86-731-84805412; Fax: +86-731-88879044; hechongxian@csu.edu.cn. Hao Pan, Department of Periodontics and Oral Mucosal Section, Xiangya Stomatological Hospital, Central South University, Changsha 410078, People's Republic of China; panhao@csu.edu.cn

Received: May 5, 2019; **Accepted:** June 4, 2019; **Published Online:** July 1, 2019

Citation: Shuai C J, Yang W J, Yang Y W, *et al.*, 2019, A continuous net-like eutectic structure enhances the corrosion resistance of Mg alloys. Int J Bioprint, 5(2): 207. http://dx.doi.org/10.18063/ijb.v5i2.207

1. Introduction

Mg alloys are potential bone implants in the orthopedic field due to their good biocompatibility, natural biodegradability, and similar density and Young's modulus to nature bone[1-5]. Compared with other Mg alloys, Mg-Al series alloys exhibit more favorable mechanical strength with the help of Al solid solution strengthening and precipitation strengthening, thus attracting intensive researches in recent years[6-8]. Witte *et al.*[9] investigated the degradation behavior and the bone response of Mg-Al series alloys, including AZ31 and AZ91. They reported that a small amount of Al released during the degradation could be tolerable. Wen *et al.*[10] investigated the corrosion behavior of Mg-Al series alloys and claimed that their corrosion resistances were closely related to Al content. Nevertheless, Mg-Al series alloys degrade rather rapidly in physical environments, because the high potential differences between *α*-Mg grains and *β* phase cause severe galvanic corrosion[9,10]. The rapid degradation results in a fast loss of mechanical strength, as well as a large amount of hydrogen accumulation and local alkalization, which significantly limits their clinical applications.

A workable strategy to improve the corrosion resistance is to change the component of the second

phase toward reducing their electrochemical nobility. For example, Baek *et al.*[11] investigated the effect of Y on the corrosion behavior of Mg-Al-Ca alloy. It was found that the Y-containing phase was less cathodic and drastically weakened the galvanic corrosion tendency. Liu *et al.*[12] reported that rare earth element enhanced the corrosion resistance of AM60, because the deposited phases containing rare earth were less cathodic than β-$Mg_{17}Al_{12}$ phase. Another strategy to increase the corrosion resistance is to ameliorate the distribution of the second phase in Mg matrix. Wu *et al.*[13] confirmed that adding proper Al into Mg-Ca alloy formed a continuous second phase, which provided barrier effect, resulting in better corrosion resistance. Shuai *et al.*[14] also reported that Nd-introduced continuous second phase enhanced the corrosion resistance of Mg matrix, with the degradation rate decreased from 5.25 to 1.56 mm/y.

In this study, Ti was introduced into AZ61 to ameliorate the characterizations of precipitates, with an aim to improve the corrosion resistance. In Al-Ti-Mg system, Ti will combine with Al to form precipitates and increase the diffusivity of Al in Mg solute, resulting in the increase of Al content near the eutectic point during the solidification process[15]. Thus, it was expected that Ti could promote the formation of less cathode eutectic α phase, which can reduce the electrode potential differences of the matrix. On the other hand, the precipitation of eutectic α phase will consume Al atoms, which is conducive to reducing the formation of β-$Mg_{17}Al_{12}$ phase, thus further alleviating the galvanic corrosion in the matrix. The microstructures, mechanical properties, and corrosion behaviors of Ti contained AZ61 alloys fabricated with selective laser melting (SLM) were systematically investigated. Moreover, the biocompatibility was also studied through *in vitro* cell culture experiments.

2. Experimental Methods

2.1 Specimens Preparation

The gas-atomized AZ61 powder (Weihao Magnesium powder Ltd., China) had a particle size distribution of d_{10}=29.04 μm, d_{50}=52.68 μm, and d_{90}=84.71 μm. The Ti powder (Naiou Nano Science and Technology Ltd., China) had a particle size varying from 20 to 50 nm. The AZ61-*x*Ti (*x*=0, 0.25, 0.5, 0.75, and 1.0 wt.%) mixed powders were prepared using a ball mill with a rotation speed of 200 rpm for 8 h under Ar atmosphere. The morphologies of mixed powders were observed using a scanning electron microscope (SEM, Phenom proX, Phenom-World BV, Netherlands) coupled with an energy dispersive spectroscopy (EDS), with results presented in Figure 1. The element mapping results corresponding to AZ61-0.5Ti mixed powders indicated Ti nanoparticles homogeneously dispersed over the AZ61 particle surface.

Cubic samples (10 × 10 × 10 mm^3) were fabricated using a SLM system equipped with an YLR-500-WC fiber laser (IPG Photonics Inc.). The process parameters were determined at a laser power of 120 W, a scanning speed of 10 mm/s, a layer thicknesses of 150 μm, a scanning spacing of 80 μm, and a spot size of 80 μm. All the experiments were performed under a high-purity Ar atmosphere. A zigzag pattern was applied to scan the powder layer.

2.2 Microstructural Characterizations

The specimens were grounded, polished, and ultrasonically cleaned with ethanol. Then, the microstructures were investigated using SEM. Moreover, the crystalline structure was observed using an optical microscope (Leica DM200, Leica Microsystems, Germany) after etching with a nitric acid alcohol solution (4%). Furthermore, the phase compositions were identified using X-ray diffraction (XRD, D8 Advance diffractometer, Bruker Inc., German) at a scanning rate of 8 min^{-1}.

2.3 Mechanical Characterizations

The SLM fabricated samples were cut into 8 mm in length and 4 mm in diameter for compressive tests. The compressive tests were carried out using a universal mechanical testing machine (Instron, USA) with a compression speed of 0.5 mm/min. Microhardness was measured on a microhardness tester with a load of 0.98 N and a holding time of 15 s. The microhardness measurements were taken 5 times for each specimen, and the distance between each adjacent indentation was 500 μm.

2.4 Electrochemical Experiments

Electrochemical experiments were performed three a three-electrode system in which the sample was used as the working electrode, a platinum foil as a counter electrode, and a saturated calomel electrode as a reference electrode. All the electrodes were connected to an electrochemical workstation (Interface 1000, Gamry Instrument, USA) and immersed in simulated body fluid (SBF) at 25±0.5°C. The SBF was prepared according to reference[16]. The open circuit potential was first monitored for 2400 s. Then, the potentiodynamic polarization testing was conducted with a scanning rate of 0.333 mV/s.

2.5 Immersion Experiments

Immersion experiments were carried out to study the corrosion behavior. Specimens were immersed in SBF at 37°C, with a volume to exposure area ratio of 20 mL cm^{-2}. The hydrogen release rate and the pH values during immersion were monitored. Meanwhile, the ion concentrations of the soaked media were measured

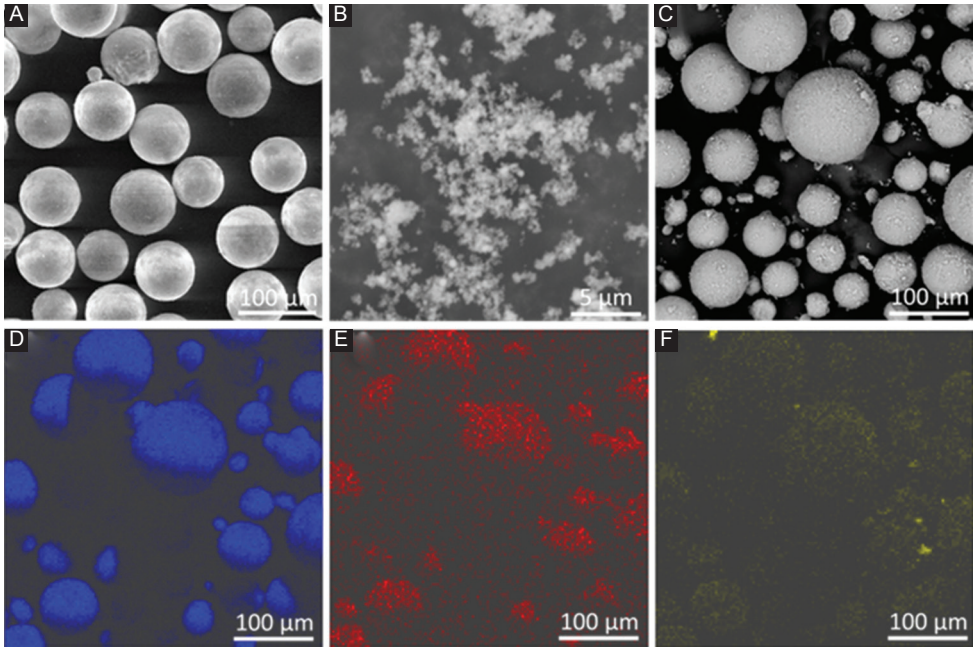

Figure 1. Morphologies of original powders: (**A**) AZ61, (**B**) Ti and (**C**) AZ61-0.5Ti mixed powder; (**D**)-(**F**) were the element distributions of Mg, Al, and Ti of AZ61-0.5Ti mixed powder.

using an inductively coupled plasma atomic emission spectroscopy (ICP-OES, PerkinElmer, Optima 5300DV, USA). The corrosion morphologies after immersion for 2 and 7 days were characterized using SEM. Besides, mass loss was obtained after removing the corrosion products in chromic acid solution (200 g/L CrO_3, 10 g/L $AgNO_3$). Then, corrosion rates (C_R) were obtained using the following equation, C_R=3.65 $\Delta W/\rho$, where ΔW was the mass loss rate (mg cm^{-2}/d) and ρ was the density (g cm^{-3}).

2.6 Cell Culture

Human osteosarcoma cells (MG63, American Type Culture Collection, USA) were employed for the cell tests. DMEM (Gibco, Grand Island, USA) supplemented with 10% fetal bovine serum (Gibco, Grand Island, USA), 100 U/mL penicillin and 100 mg/mL streptomycin (BI, Kibbutz Beit Haemek, Israel) were used as culture medium. The extracts of AZ61-Ti were prepared by immersing the samples in DMEM for 72 h. The ratio of exposed areas to solution volume was 1 cm^2/mL. The obtained 100% extracts were then diluted to 50% and 10% concentrations. The pH value and ion concentration of the extracts were also evaluated.

Cell counting kit-8 (CCK-8) assays were adopted to evaluate cell viabilities. Cells were seeded in 96-well plates at a density of 5×10^4/mL and cultured for 24 h. Then, the cell culture media were replaced by extracts (100%, 50%, and 10%). Pure DMEM was used as control. After incubating for 1, 3, and 5 days, 10 μL of CCK-8 (5 mg/ml, Sigma-Aldrich, USA) solution was added to each well for 2 h at 37°C. After that, the spectrophotometric absorbance was recorded at a wavelength of 570 nm referenced to 630 nm on a paradigm detection platform (Beckman Coulter, USA).

For LIVE/DEAD cell assay, cells were seeded in 48-well plates with extracts. At each period, the cells were gently rinsed with phosphate-buffered solution (PBS) and stained using Calcein-AM (2 μM) and ethidium homodimer-1 (4 μM). Afterward, the cells were gently washed with PBS and observed under fluorescence microscopy (Olympus, BX60, Japan).

2.7 Statistical Analysis

All the experiments in this work were repeated for 3 times. The experimental data were expressed as the average ± standard deviation. One-way analysis of variance was used to analyze the statistical analyses followed by Tukey posthoc analysis. Statistical significance was considered when P<0.05.

3. Results

3.1 Microstructure

SEM and EDS were combined to study the microstructure of the AZ61-Ti, as displayed in Figure 2. In AZ61, some β phases (bright particles) homogeneously distributed in Mg matrix (dark regions), as shown in Figure 2A. A close observation revealed that there was some divorced eutectic α phase formed along grain boundaries and interfaces. Combining with the elemental surface analysis,

the eutectic α phase was enriched in Al. With addition of 0.25 wt% Ti, more Al-enriched eutectic α phase and less β phase were observed. In AZ61-0.5Ti, the Al-enriched eutectic α phase continuously distributed and constructed a net-like structure, which was also proved by the EDS mapping results. Moreover, only a few β phase particles were observed. With Ti further increasing to 0.75 and 1.0 wt%, the β phase particles were coarsened and increased, which were enriched in Al and Ti, as revealed by EDS analysis.

The quantitative elemental compositions were obtained, as shown in Figure 2B, in which point 1, point 4, and point 7 represented position in the vicinity of the Al-enriched eutectic α phase, point 2, point 5, and point 8 represented the position in the β phase, and point 3, point 6, and point 9 represented the position in the α-Mg grains, respectively. It could be seen that the Al contents dissolved in α-Mg grains were 2.92±0.74 wt.%. With Ti increasing to 0.5 wt% and 1.0 wt%, the Al contents were dissolved in α-Mg grains gradually decreased to 1.93 ± 0.51 and 1.13 ± 0.46 at.%, respectively. Similarly, the Al content in β phase was also decreased with increasing Ti content, which was 20.46 at.% for AZ61, 10.29 at.% for AZ61-0.5Ti, and 9.08 at.% for AZ61-1.0Ti. However, the Al content in Al-enriched eutectic α phases showed a different trend. Al-enriched eutectic α phases in AZ61-0.5Ti exhibited the lowest Al content of 5.89 at.%, which was lower than that in AZ61 (6.42 at.%) and AZ61-1.0Ti (6.28 at.%). Their results indicated that the diffusivity of Al was increased with increasing Ti. Besides, Zn was detected in all of the AZ61-Ti alloys. Moreover, a small amount of Ti was detected in the β phase of AZ61-1.0Ti.

The area fraction of Al-enriched α phase and β phase was measured by the Image-Pro Plus 6.0 software, with results displayed in Table 1. The area fraction of Al-enriched eutectic α phase in AZ61 was 17.3%. With Ti gradually increased to 0.5 wt%, the area fraction of eutectic α phase gradually increased to 42.0%, which indicated that the Al atoms in Mg solute were consumed to constitute more Al-enriched eutectic α phase. With Ti further increased to 1.0 wt%, the area fraction of eutectic α phase was reduced to 27.8%. It was believed that excess Ti reacted with Al to form β phase, thus reducing the Al content in eutectic.

The optical microstructure and the calculated grain sizes of the AZ61-Ti are presented in Figures 3A-F. The grain sizes for the AZ61, AZ61-0.25Ti, AZ61-0.5Ti, AZ61-0.75Ti, and AZ61-1.0Ti were 16.4 ± 2.3, 12.7 ± 2.1, 10.4 ± 1.6, 9.5 ± 1.1, and 9.1 ± 0.8 µm, respectively, indicating that Ti significantly refined the grain sizes. The XRD patterns indicated that α-Mg was a major phase. Moreover, the β phase of AZ61, AZ61-0.25Ti, and

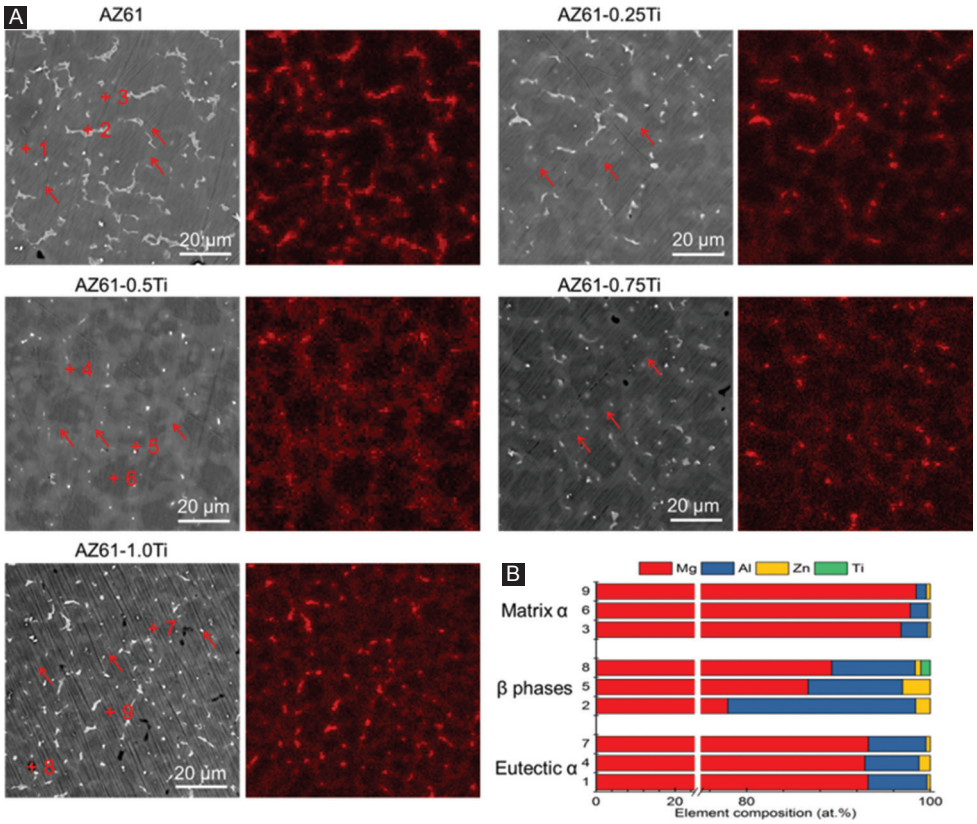

Figure 2. (**A**) Microstructure of AZ61-Ti observed under scanning electron microscope and the corresponding elemental distribution of Al; red arrow indicates the eutectic α phase. (**B**) Energy dispersive spectroscopy results corresponding to particles in Figure 2A.

Table 1. The calculated area fraction of eutectic α-Mg phase, β-phase, and matrix.

Samples	Eutectic α	β phases	Matrix
AZ61	17.3%	7.0%	75.7%
AZ61-0.25Ti	25.8%	2.1%	72.1%
AZ61-0.5Ti	42.0%	0.7%	57.3%
AZ61-0.75Ti	36.1%	1.6%	50.3%
AZ61-1.0Ti	27.8%	2.6%	69.6%

AZ61-0.5Ti was $Mg_{17}Al_{12}$ (Figure 3G). The diffraction intensities corresponding to $Mg_{17}Al_{12}$ phase decreased with increasing Ti content. Moreover, the peaks of $Mg_{17}Al_{12}$ were not detected in AZ61-1.0Ti. Meanwhile, $TiAl_3$ phase could be identified in AZ61-0.75Ti and AZ61-1.0Ti and its diffraction intensities increased with Ti content increasing.

3.2 Degradation Behavior

The open circuit potential of AZ61-Ti is given in Figure 4A. During the electrochemical test, the open circuit potential gradually increased and eventually stabilized. From the thermodynamic point of view, a higher open circuit potential indicated a more stable surface. It was believed that the increased open circuit potential was due to a protective $Mg(OH)_2$ layer formed with the dissolution of Mg matrix[17]. More importantly, AZ61-0.5Ti exhibited the highest open circuit potential.

The potentiodynamic polarization curves of the AZ61-Ti are given in Figure 4B. Moreover, the corrosion potential (E_{corr}) and cathodic polarization corrosion current density (i_{corr}) derived from the potentiodynamic polarization curves are given in Figure 4C and D. The E_{corr}, which represented the corrosion tendency, could be ranked as AZ61-0.5Ti >AZ61-0.75Ti >AZ61-0.25Ti >AZ61-1.0Ti >AZ61. Moreoverm the AZ61-0.5Ti exhibited the lowest current density of 9.2±1.4 μA·cm^{-2}. It was well known that i_{corr} mainly reflected the intensity of the chemical reaction during the electrochemical corrosion[18,19]. Thus, AZ61-0.5Ti with highest E_{corr} and smallest i_{corr} exhibited the optimal corrosion resistance.

Immersion tests were conducted to further study the corrosion behavior, with results shown in Figure 5. The hydrogen evolution curves are depicted in Figure 5A and the pH value variations are depicted in Figure 5B. Clearly, the degradation behaviors differed with Ti content. AZ61 exhibited the relatively fast hydrogen release and pH increase. When Ti was incorporated, the released hydrogen decreased and the increase rate of pH slowed down. The AZ61-0.5Ti exhibited the least hydrogen evolution volume and the lowest pH compared with other investigated alloys. However, the hydrogen volumes and pH were rapidly increased in AZ61-0.75Ti and AZ61-1.0Ti, implying that the excessive Ti decreased the corrosion resistance.

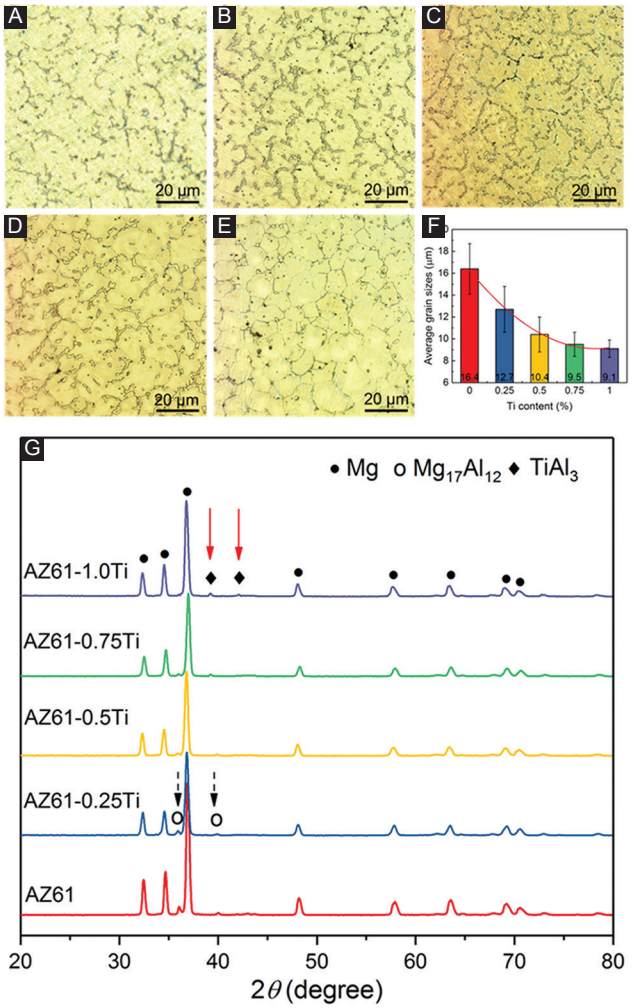

Figure 3. Optical microstructure of (**A**) AZ61, (**B**) AZ61-0.25Ti, (**C**) AZ61-0.5Ti, (**D**)AZ61-0.75Ti, and (**E**) AZ61-1.0Ti. (**F**) The measured average grain sizes. (**G**) X-ray diffraction patterns of AZ61-Ti. $Mg_{17}Al_{12}$ and $TiAl_3$ phases were marked by black dash arrow and red solid arrow, respectively.

The variation of Mg ion-releasing behavior during immersion was similar to that of the hydrogen evolution volume and pH variation (Figure 5C). Mg^{2+} concentrations tended to increase with immersion time increasing, indicating the dissolution of specimens. AZ61-0.5Ti released the least amount of Mg^{2+}, indicating it has the slowest degradation rate. The C_R calculated by mass loss exhibited a similar trend to that of the Mg ion-releasing (Figure 5D). All the immersion tests demonstrated that AZ61-0.5Ti had the best corrosion resistance.

The typical corrosion morphologies and composition analyses of the corrosion product are displayed in Figure 6. A corrosion product layer was formed on the specimen with some particles deposition. A lot of micro-

cracks appeared on the surface were due to the shrinkage of the corrosion product layer during dehydration. It was obvious that AZ61 suffered the most severe corrosion, which was consistent with its fastest degradation rate (Figure 6A). As a comparison, AZ61-0.5Ti suffered homogeneous corrosion, as depicted in Figure 6C. Some particles were deposited on this layer, which was enriched in Mg, Ca, P, C, and O (area 2), with a higher content of Ca and P than that on area 1 (Figure 6F). Nevertheless, AZ61-0.75Ti and AZ61-1.0Ti both suffered severely localized corrosion. With increasing immersion period to 7 days, the AZ61-0.5Ti was also compact, except for some micro-cracks and particles on the surface. Large cracks and flaking of corrosion product could be observed on AZ61 and AZ61-1.0Ti. The flaking of corrosion products resulted from the thickening of the corrosion layer and dehydration process[20].

3.3 Cytotoxicity

The pH and ion concentration of the extracts during the 72 h incubation is summarized in Figures 7A and B. There were no significant differences in the pH of the 100% extracts (all closing to 9). The pH only slightly reduced in 50% extracts due to the buffer effect of the culture medium. When further diluted to 10%, the pH values were decreased to 7.89 (Figure 7A). The Mg^{2+} releasing during the incubation reflected the degradation rate of AZ61-Ti in the culture medium. AZ61-0.5Ti showed the lowest Mg^{2+} concentration, indicating its optimal corrosion resistance. The Zn^{2+} concentrations in the extracts were in the single-digit μg/mL range (Figure 7B). In addition, Al^{3+} concentrations in all the extracts were not detected, due to the small solubility products of aluminum hydroxide (1.3×10^{-33})[21].

The cell viability of the MG63 incubated in AZ61-Ti extracts is depicted in Figure 7c. After 3 days' culture, all the undiluted extracts (100%) resulted in a significantly reduced cell viability compared to the negative control. However, the toxic effects could be mitigated by dilution. The cell viability was about 90% for AZ61-0.5Ti in 50% extracts, suggesting the AZ61-0.5Ti alloy had good cell compatibility. The cell viability level was further improved with 10% extract dilution. The cell viability was improved with extract dilution which may be in consonance with the clinical condition in which the material becomes diluted with the surrounding tissue fluid[22]. According to ISO 10993-5, all the samples showed acceptable cell viabilities, which were higher than 80%[23-25].

LIVE/DEAD staining assay was further used to evaluate the biocompatibility (Figure 8). Obviously, all

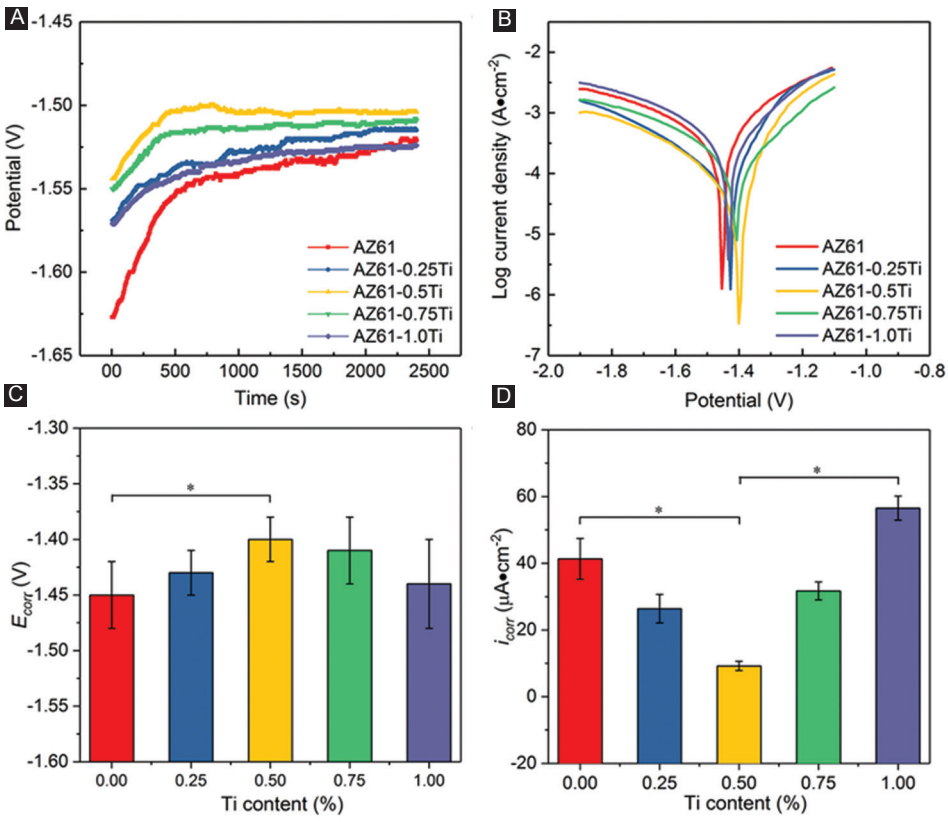

Figure 4. Electrochemical testing results of AZ61-Ti: (**A**) open circuit potential curves, (**B**) potentiodynamic polarization curves, (**C**) E_{corr} and (**D**) i_{corr} derived from the potentiodynamic polarization curves by Tafel extrapolation.

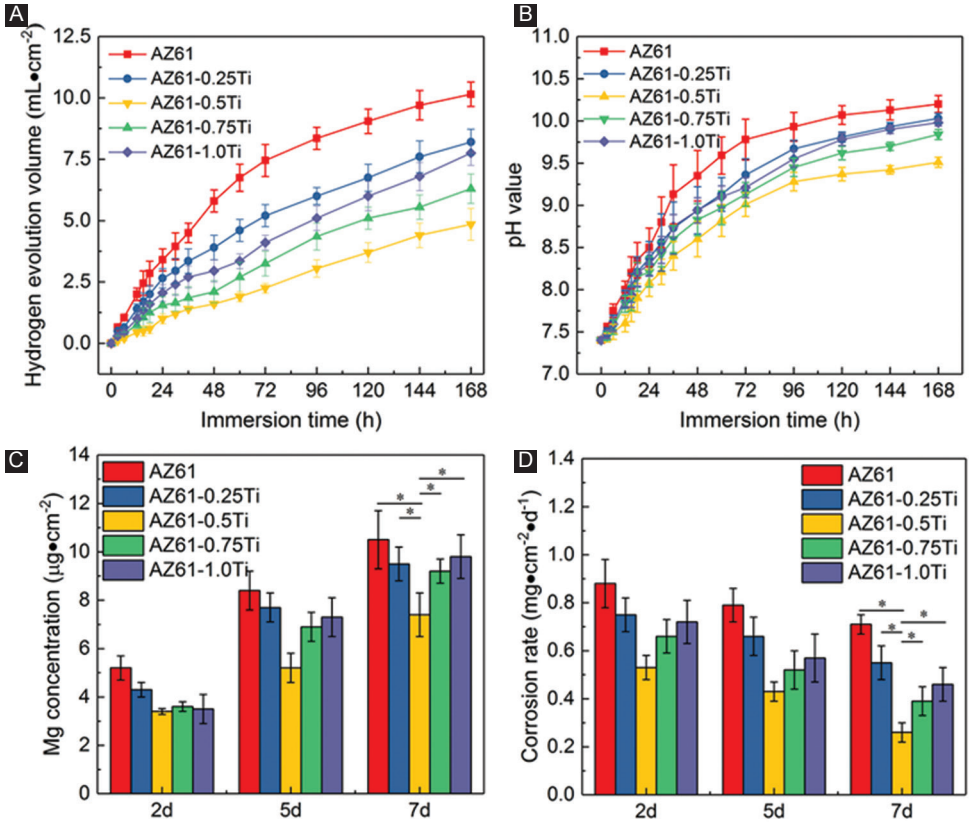

Figure 5. Immersion degradation behaviors of AZ61-Ti: (**A**) Hydrogen evolution volumes, (**B**) pH during immersion, (**C**) ion-releasing behavior during immersion, and (**D**) corrosion rate calculated from the mass loss.

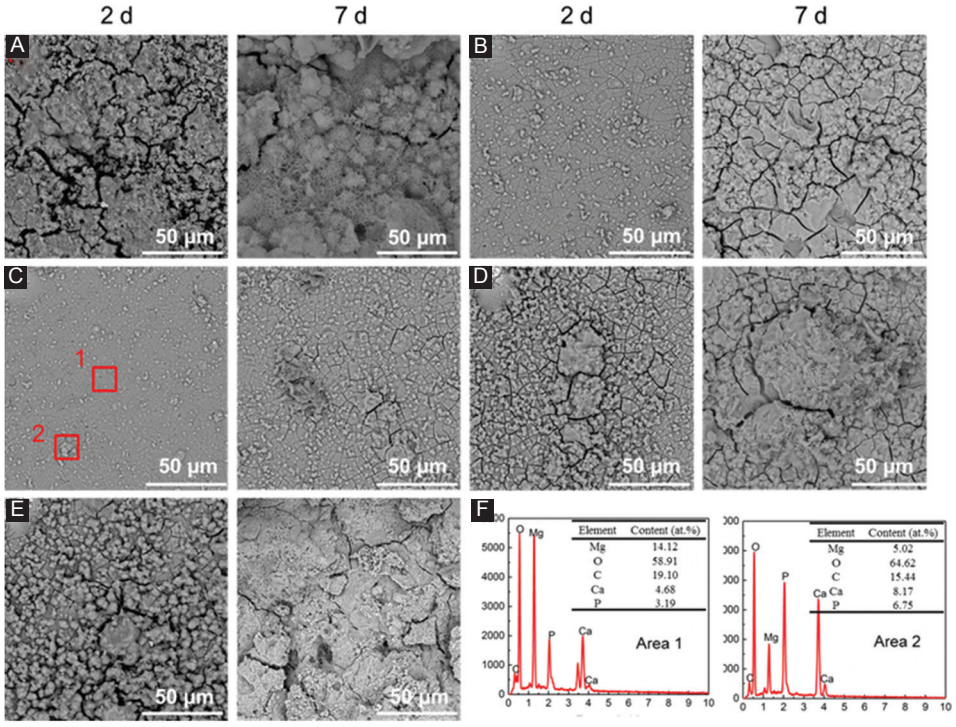

Figure 6. Corrosion surfaces of (**A**) AZ61, (**B**) AZ61-0.25Ti, (**C**) AZ61-0.5Ti, (**D**) AZ61-0.75Ti, and (**E**) AZ61-1.0Ti observed under scanning electron microscope after immersion for 2 and 7 days; (**F**) energy dispersive spectroscopy results of specific areas in AZ61-0.5Ti.

the AZ61-Ti extracts exhibited improved cell viability compared with AZ61 as the cell density (number of cells) was enhanced. Specifically, AZ61-0.5Ti exhibited the best cell viability. There were few apoptotic cells (red fluorescence in the nuclei) in each group for all culture periods. Moreover, cells exhibited similar shape after culturing for 24 h and 72 h. Clearly, AZ61-0.5Ti exhibited improved biocompatibility as compared with AZ61. It was believed that the enhanced corrosion resistance should be responsible for the improved biocompatibility[26]. For AZ61-0.5Ti, the enhanced corrosion resistance resulted in a reduced degradation rate, thus decreasing the corrosion products, which might alleviate the cytotoxicity[27].

3.4 Mechanical Properties

The compressive strength and microhardness of AZ61-Ti are displayed in Figure 9. AZ61 exhibited a relatively low compressive strength of 110.4 ± 15.2 MPa. With Ti gradually increasing to 0.5 wt%, the compressive strength was gradually improved to 175.6±21.3 MPa. However, with Ti content further increasing to 0.75 wt% and 1.0 wt%, the compressive strength was decreased to 145.3 ± 30.9 MPa and 123.9 ± 34.7 MPa, respectively. AZ61 had a relatively low microhardness of 84.8 ± 3.7 HV. With the increase of Ti, the microhardness gradually increased to 90.1 ± 4.0 HV for AZ61-0.25Ti, 95.2 ± 3.4 HV for AZ61-0.5Ti, 96.3 ± 3.1 HV for AZ61-0.75Ti, and 97.8 ± 4.3 HV for AZ61-1.0Ti, respectively (Figure 9B).

4. Discussion

4.1 Microstructure and Mechanical Properties

In the present study, the incorporation of moderate Ti induced the formation of continuous net-like eutectic α phase. It was believed that Ti, which had low solid solubility in Mg, would be first rejected into the interdendritic liquid phase during the solidification of the molten pool[28]. From the perspective of thermodynamics, Ti in the interdendritic liquid would catch the Al atoms in Mg solute to form the second phase due to the high affinity between Ti and Al[15]. Thus, the diffusivity of Al would be enhanced during the solidification, resulting in an increased Al content near the eutectic location. With the liquid phase cooling to the eutectic temperature and the Al content close to eutectic composition, the eutectic reaction would occur to form the eutectic phases.

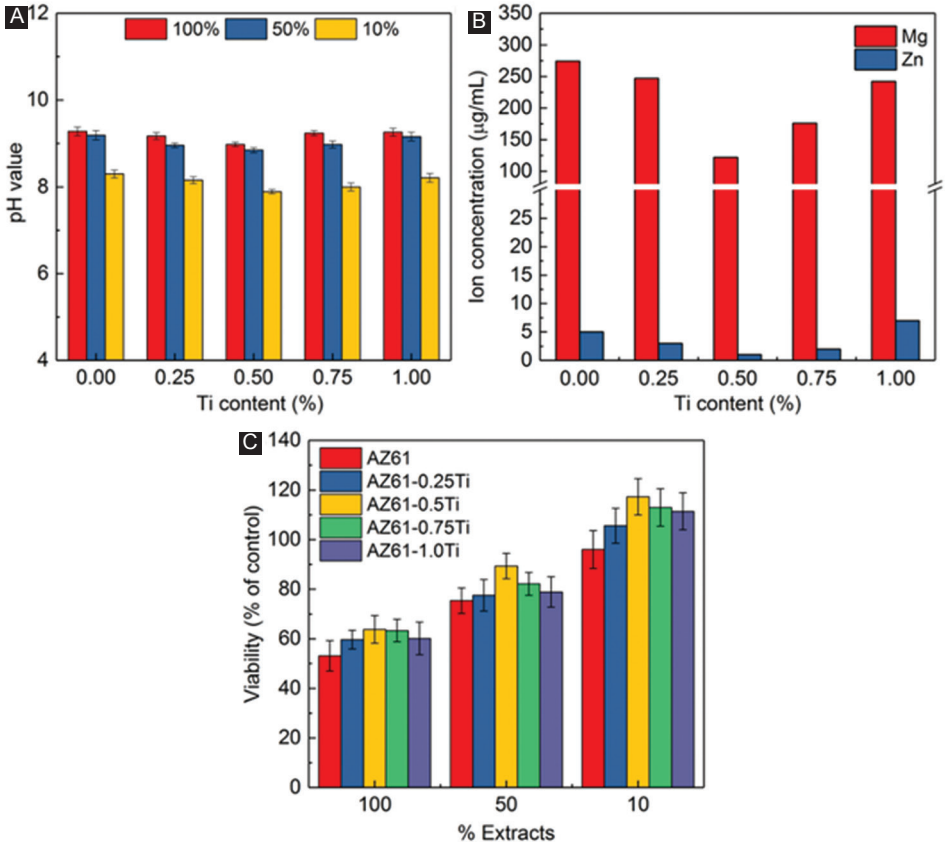

Figure 7. (**A**) pH of the extracts; (**B**) Mg and Zn concentration in the extracts; (**C**) relative viability of MG63 cells culture in AZ61-Ti extracts.

On the other hand, the rapid solidification occurred in SLM also played a key role in the formation of continuous net-like eutectic α phase. According to the Mg-Al binary equilibrium phase diagram[29], the maximum solid solubility of Al in α-Mg is about 12.7 wt% at the eutectic temperature of 437°C and its solid solubility at room temperature is about 2 wt%. In the present study, SLM, which involved a fast cooling rate, was applied to fabricate AZ61-Ti alloy. Moreover, such a rapid solidification was believed to promote the occurrence of eutectic reaction at lower eutectic temperature and critical hypoeutectic Al content (as compared with equilibrium). The eutectic reaction precipitated the eutectic α phase and eutectic β particles, which would attach to the primary α-Mg grains and distribute in grain boundaries, respectively. Moreover, the fast cooling rate was conducive for the homogeneous precipitation of the eutectic α phase and eutectic β particles. Therefore, the eutectic α phase distributed continuously and formed a net-like structure along the grain boundaries.

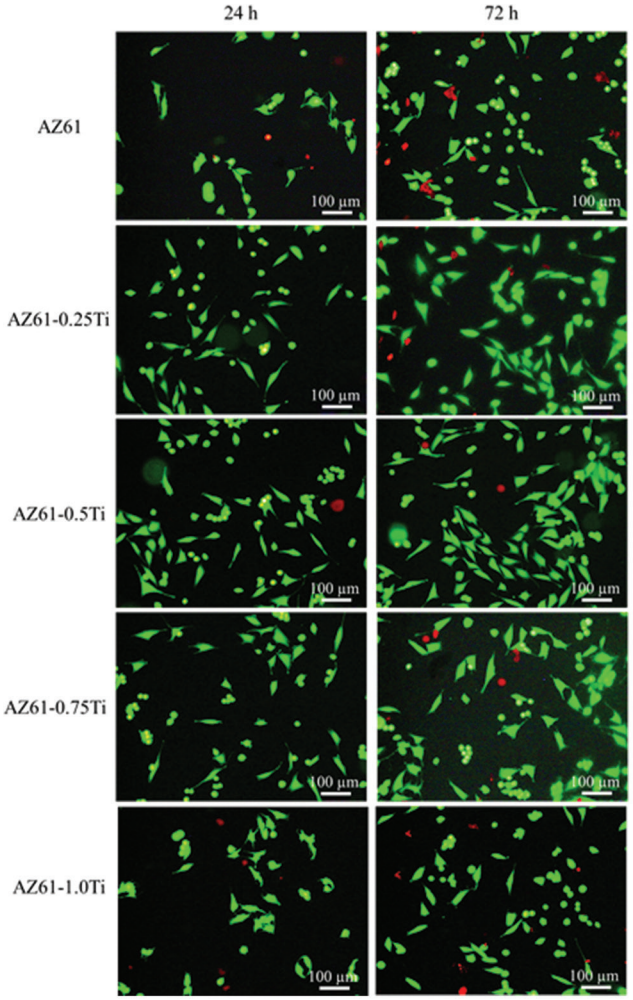

Figure 8. LIVE/DEAD staining of MG63 cells seeded in AZ61-Ti 100% extracts for 24 h and 72 h.

Impacts of Ti on the grain sizes were also observed in this study. In Ti containing Mg-Al alloys, Ti element served as a surface active element, which could significantly reduce the alloy solid-liquid interfacial tension and decrease the nucleation energy during the solidification process[30]. According to the nucleation formula, $r^*=-2\sigma_{LS}/\Delta G_m$;[31] where r* was the critical nucleation radius, σ_{LS} was the solid-liquid interfacial tension, and ΔG_m was the Gibbs free energy of solidification. Ti reduced the solid-liquid interfacial tension, thereby reducing the critical nucleation radius. As a result, the ultimately nuclear volume of the primary α-Mg was improved, thus forming refined grain size. Furthermore, in AZ61-0.75Ti and AZ61-1.0Ti, excessive Ti combined with Al to form the $TiAl_3$ phase. Although the $TiAl_3$ phase was not regarded as the core of crystal formation, it would be pushed to the front of solid-liquid interfaces and prevented the grain growth. Therefore, the grain sizes decreased continuously with increasing Ti content.

4.2 Corrosion Behaviors

It is known that an ideal bone implant should progressively degrade at a suitable rate (approximately

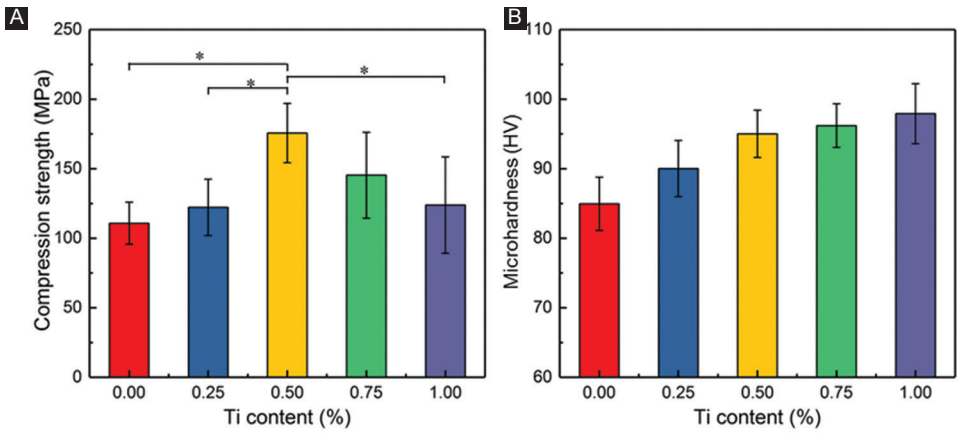

Figure 9. Mechanical performances of AZ61-Ti: (**A**) Compression strength and (**B**) microhardness.

0.2~0.5 mm/year) to match the bone healing process. In the present work, the degradation rate of AZ61 alloy was dramatically decreased from 0.74 (1.56 mm/year) to 0.24 $mg \cdot cm^{-2}/d^{-1}$ (0.51 mm/year[1]) after adding 0.5 wt% Ti. The improved corrosion resistance could be explained from two aspects as follows. On the one hand, Ti promoted the formation of divorced eutectic α phase and reduced the formation of divorced β-$Mg_{17}Al_{12}$ phase. Significantly, the potential difference between the eutectic α phase and α-Mg grains was slighter than that between β-$Mg_{17}Al_{12}$ phases and α-Mg grains, due to the lower potential of eutectic α phase[32] and a reduced potential difference would decrease the susceptibility to galvanic corrosion of AZ61-0.5Ti.

On the other hand, the continuous net-like eutectic α phase also did a favor for the enhanced corrosion resistance. During degradation, the α-Mg grains dissolved preferentially, leaving the eutectic α phase on the surface[33]. Al-enriched eutectic α phase was relatively inert in the physiological environment. Thus, the exposed eutectic α phase would act as a barrier and retard the corrosion to a certain extent. For AZ61 and AZ61-0.25Ti, the discontinuous eutectic α phase did not form an effective barrier to corrosion attack, as shown in Figure 2. Resultantly, the AZ61-0.5Ti exhibited higher corrosion resistance compared with AZ61 and AZ61-0.25Ti.

It should be noted that with Ti further increasing to 1 wt%, the $TiAl_3$ phase precipitated in grain boundary (Figure 2), which exhibited higher potential difference with α-Mg grains than that between the eutectic α phase and α-Mg grains. Hence, the $TiAl_3$ phase was considered as the cathode and form galvanic cells with α-Mg grains, resulting in dramatically galvanic corrosion. Thus, the galvanic corrosion was considerably enhanced, which decreased corrosion resistance of AZ61-1.0Ti.

4.3 Mechanical Properties

Mechanical properties were closely related to microstructure. In the present study, AZ61-Ti exhibited equiaxed grains with eutectic α and β phases on the interdendritic regions (Figure 2). The formation of the Al-enriched eutectic α phase was a solid solution of Al in α-Mg phase, which caused a negative deformation of the lattice structure and increased the dislocations resistance that occurred in grains[34,35]. Moreover, the addition of Ti significantly refined the grains, increased the grain boundaries, and suppressed the formation of β phase. Resultantly, the crack tendency and the fracture propagation were reduced. Thus, the compressive strength of AZ61-Ti was improved. However, as Ti was more than 0.5 wt%, the coarse $TiAl_3$ particles precipitated and aggregated at the grain boundaries, which broke the connection between the adjacent grains. As external force was applied to specimen, stress concentration, and porous around the $TiAl_3$ particles would form, which made the alloys easily to crack in the grain boundary, resulting in reduced compressive strength[36]. The microhardness of AZ61-Ti was increased with the increase of Ti content, which could be attributed to the fine grain strengthening. Besides, the eutectic α and β phases had higher microhardness than α-Mg matrix, which could also contribute to the increase of microhardness.

5. Conclusions

In this study, Ti-introduced AZ61 alloy was fabricated with SLM to enhance the corrosion resistance. Results indicated that Ti promoted the formation of eutectic α-Mg phase and reduced the formation of β-$Mg_{17}Al_{12}$ phase. When the Ti content reached to 0.5 wt%, the eutectic α-Mg phase formed a continuous net-like structure providing resistance for α-Mg matrix. Polarization test, hydrogen evolution, pH value, Mg^{2+} concentration, and mass loss suggested that AZ61-0.5Ti exhibited the optimal corrosion resistance. The typical corrosion morphologies demonstrated that the AZ61-0.5Ti suffered uniform corrosion. Besides, AZ61-0.5Ti showed improved compressive strength and microhardness compared to AZ61 due to solid solution strengthening and fine-grain strengthening. In addition, the Ti contained Mg alloys exhibited good cytocompatibility.

Acknowledgment

This study was supported by the following funds: (1) The natural science foundation of China (81871494, 81871498, 51705540); (2) Hunan provincial natural science foundation of China (2018JJ3671, 2019JJ50588); (3) Guangdong province higher vocational colleges and schools pearl river scholar funded scheme (2018); (4) The open sharing fund for the large-scale instruments and equipments of central South university; (5) The project of hunan provincial science and technology plan (2017RS3008); Shenzhen science and technology plan project (JCYJ20170817112445033); (6) National postdoctoral program for innovative talents (BX201700291); (7) The China postdoctoral science foundation (2018M632983); (8) The fundamental research funds for the central universities of central South University (2019zzts005).

References

1. Staiger M, Pietak A, Huadmai J, *et al.*, 2006, Magnesium and its Alloys as Orthopedic Biomaterials: A Review. *Biomaterials*, 27:1728-34. DOI 10.1016/j.biomaterials.2005.10.003.
2. Zhao D, Witte F, Lu F, *et al.*, 2017, Current Status on Clinical Applications of Magnesium-based Orthopaedic Implants: A Review from Clinical Translational

Perspective. *Biomaterials*, 112:287-302. DOI 10.1016/j.biomaterials.2016.10.017.

3. Gao C, Feng P, Peng S, *et al.*, 2017, Carbon Nanotube, Graphene and Boron Nitride Nanotube Reinforced Bioactive Ceramics for Bone Repair. *Acta Biomater*, 61:1-20. DOI 10.1016/j.actbio.2017.05.020.
4. Abidin NIZ, Da Forno A, Bestetti M, *et al.*, 2015, Evaluation of Coatings for Mg Alloys for Biomedical Applications. *Adv Eng Mater*, 17(1):58-67. DOI 10.1002/adem.201300516.
5. Shuai C, Li S, Peng S, *et al.*, 2019, Biodegradable Metallic Bone Implants. *Mater Chem Front*, 3:544-62.
6. Chai Y, Jiang B, Song J, *et al.*, 2018, Role of Al content on the Microstructure, Texture and Mechanical Properties of Mg-3.5 Ca Based Alloys. *Mater Sci Eng A*, 730:303-16.
7. Zheng YF, Gu XN, Witte F, 2014, Biodegradable Metals. *Mater Sci Eng R*, 77:1-34.
8. Cheng W, Bai Y, Wang L, *et al.*, 2018, Strengthening Effect of Extruded Mg-8Sn-2Zn-2Al Alloy: Influence of Micro and Nano-Size Mg-Sn Precipitates. *Materials,* 10(7):822. DOI 10.3390/ma10070822.
9. Witte F, Kaese V, Haferkamp H, *et al.*, 2005, *In vivo* Corrosion of Four Magnesium Alloys and the Associated Bone Response. *Biomaterials*, 26(17):3557-63. DOI 10.1016/j.biomaterials.2004.09.049.
10. Wen Z, Wu C, Dai C, *et al.*, 2009, Corrosion Behaviors of Mg and its Alloys with Different Al contents in a Modified Simulated Body Fluid. *J Alloys Compd*, 488(1):392-9. DOI 10.1016/j.jallcom.2009.08.147.
11. Baek SM, Kang JS, Shin HJ, *et al.*, 2017, Role of Alloyed Y in Improving the Corrosion Resistance of Extruded Mg–Al–Ca-based Alloy. *Corros Sci*, 118:227-32. DOI 10.1016/j.corsci.2017.01.022.
12. Liu W, Cao F, Chang L, *et al.*, 2009, Effect of Rare Earth Element Ce and La on Corrosion Behavior of AM60 Magnesium Alloy. *Corros Sci*, 51:1334-43. DOI 10.1016/j.corsci.2009.03.018.
13. Wu PP, Xu FJ, Deng KK, *et al.*, 2017, Effect of Extrusion on Corrosion Properties of Mg-2Ca-χAl (χ = 0, 2, 3, 5) Alloys. *Corros Sci*, 127:280-90. DOI 10.1016/j.corsci.2017.08.014.
14. Shuai C, Yang Y, Peng S, *et al.*, 2017, Nd-induced Honeycomb Structure of Intermetallic Phase Enhances the Corrosion Resistance of Mg Alloys for Bone Implants. *J Mater Sci Mater Med,* 28(9):130. DOI 10.1007/s10856-017-5945-0.
15. Ai X, Quan G, 2012, Effect of Ti on the Mechanical Properties and Corrosion of Cast AZ91 Magnesium Alloy. *Open Mater Sci J*, 6:6-13.
16. Feng P, Wu P, Gao C, *et al.,* 2018, A Multimaterial Scaffold with Tunable Properties: Toward Bone Tissue Repair. *Adv Sci*, 5(6):1700817. DOI 10.1002/advs.201700817.
17. Li Z, Gu X, Lou S, *et al.*, 2008, The Development of Binary Mg–Ca Alloys for Use as Biodegradable Materials within Bone. *Biomaterials*, 29:1329-44. DOI 10.1016/j.biomaterials.2007.12.021.
18. Shuai C, Wang B, Yang Y, *et al.*, 2019, 3D Honeycomb Nanostructure-encapsulated Magnesium Alloys with Superior Corrosion Resistance and Mechanical Properties. *Compos B*, 162:611-20. DOI 10.1016/j.compositesb.2019.01.031.
19. Lothe J, Pound GM, 1962, Reconsiderations of Nucleation Theory. *J Chem Phys*, 36:2080-5.
20. Bian D, Deng J, Li N, *et al.,* 2018, *In Vitro* and *In Vivo* Studies on Biomedical Magnesium Low-alloying with Elements Gadolinium and Zinc for Orthopedic Implant Applications. *ACS Appl Mater Interfaces*, 10:4394-408. DOI 10.1021/acsami.7b15498.
21. Mochizuki A, Yahata C, Takai H, 2016, Cytocompatibility of Magnesium and AZ31 Alloy with Three Types of Cell Lines using a Direct *In Vitro* Method. *J Mater Sci Mater Med*, 27:145. DOI 10.1007/s10856-016-5762-x.
22. Shuai C, Guo W, Wu P, *et al.*, 2018, A Graphene Oxide-Ag co-dispersing Nanosystem: Dual Synergistic Effects on Antibacterial Activities and Mechanical Properties of Polymer Scaffolds. *Chem Eng J*, 347:322-33. DOI 10.1016/j.cej.2018.04.092.
23. International Organization for Standardization, 2009, ISO 10993-5:2009(E). Biological Evaluation of Medical Devices-Part 5: Tests for *In Vitro* Cytotoxicity. Geneva: International Organization for Standardization.
24. Shuai C, Li Y, Wang G, *et al.*, 2019, Surface Modification of Nanodiamond: Toward the Dispersion of Reinforced Phase in Poly-l-lactic Acid Scaffolds. *Int J Biol Macromol*, 126:1116-24. DOI 10.1016/j.ijbiomac.2019.01.004.
25. Shuai C, Xu Y, Feng P, *et al.*, 2019, Antibacterial Polymer Scaffold Based on Mesoporous Bioactive Glass Loaded with *In Situ* Grown Silver. *Chem Eng J*, 374:304-15. DOI 10.1016/j.cej.2019.03.273.
26. Shuai C, Cheng Y, Yang Y, *et al.*, 2019, Laser Additive Manufacturing of Zn-2Al Part for Bone Repair: Formability, Microstructure and Properties. *J Alloys Compd*, 798:606-15. DOI 10.1016/j.jallcom.2019.05.278.
27. Feng P, He J, Peng S, *et al.,* 2019, Characterizations and Interfacial Reinforcement Mechanisms of Multicomponent Biopolymer Based Scaffold. *Mater Sci Eng C*, 100:809-25.
28. Monas A, Shchyglo O, Kim SJ, *et al.*, 2015, Divorced Eutectic Solidification of Mg-Al Alloys. *JOM*, 67:1805-11.

DOI 10.1007/s11837-015-1418-4.

29. Liang G, Schulz R, 2003, Synthesis of Mg-Ti Alloy by Mechanical Alloying. *J Mater Sci*, 38:1179-84.
30. Xie D, Zhao J, Qi Y, *et al.*, 2013, Decreasing Pores in a Laser Cladding Layer with Pulsed Current. *Chin Opt Lett*, 11:111401. DOI 10.3788/col201311.111401.
31. Choi HY, Kim WJ, 2017, The Improvement of Corrosion Resistance of AZ91 Magnesium Alloy through Development of Dense and Tight Network Structure of Al-rich α Phase by Addition of a Trace amount of Ti. *J Alloys Compd*, 696:736-45. DOI 10.1016/j.jallcom.2016.11.215.
32. Mathieu S, Rapin C, Steinmetz J, *et al.*, 2003, A Corrosion Study of the Main Constituent Phases of AZ91 Magnesium Alloys. *Corros Sci*, 45:2741-55. DOI 10.1016/s0010-938x(03)00109-4.
33. Prabhu DB, Dhamotharan S, Sathishkumar G, *et al.*, 2018, Stress Corrosion Cracking of Biodegradable Mg-4Zn Alloy in Simulated Body Fluid at Different Strain Rates–a Fractographic Investigation. *Mater Sci Eng A*, 730:223-31. DOI 10.1016/j.msea.2018.06.002.
34. Wang F, Hu T, Zhang Y, *et al.*, 2017, Effects of Al and Zn Contents on the Microstructure and Mechanical Properties of Mg-Al-Zn-Ca Magnesium Alloys. *Mater Sci Eng A*, 704:57-65. DOI 10.1016/j.msea.2017.07.060.
35. Fu K, Wang J, Qiu M, *et al.*, 2018, Effects of Cold Rolling on Microstructural Evolution and Mechanical Properties of Mg–14Li–1Zn Alloy. *Adv Eng Mater*, 21:1801344. DOI 10.1002/adem.201801344.
36. Shuai C, Zan J, Qi F, *et al.*, 2019, nMgO-incorporated PLLA Bone Scaffolds: Enhanced Crystallinity and Neutralized Acidic Products. *Mater Des,* 174:107801. DOI 10.1016/j.matdes.2019.107801.